

One-pot synthesis of highly conductive nickel-rich phosphide/CNTs hybrid as a polar sulfur host for high-rate and long-cycle Li-S battery

Xiao-Fei Yu, Dong-Xu Tian, Wen-Cui Li, Bin He, Yu Zhang, Zhi-Yuan Chen, and An-Hui Lu (✉)

State Key Laboratory of Fine Chemicals, School of Chemical Engineering, Dalian University of Technology, Dalian 116024, China

© Tsinghua University Press and Springer-Verlag GmbH Germany, part of Springer Nature 2019

Received: 3 January 2019 / Revised: 25 February 2019 / Accepted: 12 March 2019

ABSTRACT

Lithium sulfur battery has been identified as a promising candidate for next storage devices attributing to ultrahigh energy density. However, non-conductive nature of sulfur and shuttling effect of soluble lithium polysulfides are intractable remaining problems. Herein, we develop a highly conductive nickel-rich Ni₁₂P₅/CNTs hybrid with high specific surface area as sulfur host to address these issues. The polar nature of Ni₁₂P₅/CNTs can significantly relieve the shuttle effect by means of a strong affinity towards lithium polysulfides and enhance kinetics of polysulfides redox reactions. In addition, the Ni₁₂P₅/CNTs with a superior conductivity (500 S·m⁻¹) and high surface area of 395 m²·g⁻¹ enables the effective electron transfer and expedited interfacial reaction. As a result, Ni₁₂P₅/CNTs hosted sulfur cathode exhibits high rate capability (784 mAh·g⁻¹ at 4 C) and stable cycling performance with a negligible capacity fading of 0.057 % per cycle over 1,000 cycles at 0.5 C. This work paves an alternative way for designing high performance sulfur cathodes involved metal-rich phosphides.

KEYWORDS

Ni-rich phosphides, carbon nanotube, high conductivity, catalytic effect, lithium sulfur battery

1 Introduction

With urgent demands for advanced energy-storage devices, lithium sulfur (Li-S) battery has attracted widespread attention because of the superior theoretical specific capacity (1,675 mAh·g⁻¹) and high energy density (2,600 Wh·kg⁻¹) [1–3]. In addition, the natural abundance, eco-friendliness and bargain price of sulfur resources also make Li-S battery a promising candidate to take place of current lithium-ion batteries [4, 5]. However, there are several key barriers to be overcome for the commercialization of Li-S battery [6, 7]. One main obstacle is non-conductive nature of sulfur [8] which retards the electron transfer and limits the utilization of sulfur, consequently causing poor rate performance. Shuttle effect is another challenge [9] because intermediate polysulfides (LiPS, Li₂S₄-Li₂S₈) can easily dissolve into the organic electrolyte and migrate between electrodes, which raises many problems, such as the wastage of active substance and the erosion of Li metal. Hence, Li-S battery shows ungratified electrochemical performance with poor rate capability, low capacity retention, and decreased Coulombic efficiency [10].

The tremendous effort has been paid to optimizing sulfur-based cathodes to boost rate performance and prolong the lifespan of Li-S battery [11]. Nanostructured carbon materials, such as graphene [12, 13], carbon nanotubes [14, 15], and porous carbon (carbon fibers [16, 17], hollow carbon spheres [18, 19], and peapod-like carbon [20]) have been reported to date as sulfur host materials because of their high specific surface area (SSA) and pore volume associated with high conductivity. Nonetheless, the interaction between those nonpolar carbon materials and polar sulfur species is so weak that LiPS can easily be exfoliated during long term cycling. Soon afterwards, heteroatom-doped carbons have been proposed, such as N [21], B [22], O [23], S [24] and P [25], which can bind

polysulfides via chemical bonds, providing the sufficient adsorption sites and robust chemisorption on polysulfides. Lately, lots of metal oxides such as MnO₂ [26], TiO₂ [27, 28], CeO₂ [29], and Nb₂O₅ [30] have already been confirmed as polar LiPS traps through chemical bonding, resulting in good electrical performance. Nevertheless, most of these polar metal compounds possess low SSA (< 100 m²·g⁻¹), maybe making them not suitable for trapping plenty of LiPSs and providing sufficient accommodation space for polysulfides conversion. Consequently, the unanchored LiPS can easily diffuse into the electrolyte, inducing the shuttle effect. Therefore, to design and engineer sulfur host materials that not only having firm adsorption with polysulfides but also possessing high specific surface area is an appropriate way to achieve outstanding capability of lithium sulfur batteries.

On the other hand, a majority of polar metal compounds possess low conductivity, impeding the electron transfer, which results in limited sulfur utilization and poor rate performance. Cui group has also reported that trapping polysulfides on insulating materials would cause accumulation of sulfur species in nonconducting areas and accelerate the capacity decay [31]. Thus, the sulfur host materials combining the ability to trap polysulfides with a high conducting property are preferable to regulate electrochemical reaction. Nickel-rich phosphides are good conductors of electricity (conductivity > 5,000 S·cm⁻¹) similar to metals [32]. By referring to the literature [33], the increasing Ni content will enhance the conductivity of nickel phosphides. Accordingly, it can be concluded that the conductivity of nickel-rich Ni₁₂P₅ is higher than Ni₂P. Therefore, nickel-rich Ni₁₂P₅, with metal-like behavior and intrinsic polarity, is beneficial for adsorbing a great amount of polysulfides and accelerating the redox reaction. If a conductive and polar host with high surface area is available, Li-S battery may achieve high rate performance and long cycling durability.

In this work, we synthesize a highly conductive nickel-rich Ni₁₂P₅/CNTs hybrid with high SSA of 395 m²·g⁻¹. This hybrid features with multiple functions including a dramatical increase of the conductivity of sulfur cathode, a strong affinity for LiPS, enhanced redox kinetics of polysulfides and abundant surface area for polysulfides conversion. Therefore, with the combined effects of Ni₁₂P₅/CNTs composite, the sulfur cathode exhibits high rate capability (784 mAh·g⁻¹ at 4 C) and stable cycling performance (capacity decay of 0.057% per cycle over 1,000 cycles at 0.5 C), which improves rate performance and cycling capability of Li-S batteries.

2 Experimental

Materials: Nickel acetate tetrahydrate (Ni(Ac)₂·4H₂O), triphenylphosphine (TPP), melamine and ethanol were all purchased from Sinopharm Chemical Reagent Co., Ltd. (Shanghai, China). Sulfur was purchased from Alfa Aesar.

2.1 Synthesis of Ni₁₂P₅/CNTs and Ni/CNTs

In a general process, 2 mmol Ni(Ac)₂·4H₂O was dissolved in 40 mL ethanol under stirring. Then 4 mmol TPP was put in the slurry and kept stirring until it became soluble. Next, 0.03 mol melamine was added to the aforementioned solution and ethanol was removed by rotary evaporation. Finally, the pale green mixture was obtained and transferred into a tube furnace and treated at 850 °C in an argon atmosphere for 2 h with 5 °C·min⁻¹ to obtain Ni₁₂P₅/CNTs. After the carbonization, the sample was treated with muriatic acid (3 M, 40 mL) under stirring for 24 h at room temperature to remove redundant nickel particles. Preparing control sample Ni/CNTs was similar to the Ni₁₂P₅/CNTs synthesis except for the use of TPP.

2.2 Synthesis of Ni₁₂P₅/CNTs-S and Ni/CNTs-S

The as-prepared Ni₁₂P₅/CNTs and sulfur were ground together by a ratio of 1:2 and heated at 155 °C in a sealed tube, maintaining 12 h for sulfur diffusing into carbon matrix via a typical melt-diffusion strategy. Preparing control sample Ni/CNTs-S was the same as the Ni₁₂P₅/CNTs-S synthesis.

2.3 Materials characterization

The feature and texture of samples were characterized by scanning electron microscopy (SEM, FEI Nova NanoSEM 450) and transmission electron microscope (TEM, FEI Tecnai F30). A thermogravimetric analyzer (NETZSCH STA449F3) was applied under an air flow with 10 °C·min⁻¹. Nitrogen adsorption isotherms were measured at 77.4 K with a Tristar 3000 analyzer (Micromeritics Instruments, USA). The Brunauer-Emmett-Teller (BET) and Barrett-Joyner-Halenda (BJH) methods were used to calculate the SSA and pore size distributions, respectively. X-ray diffraction (XRD) was measured on a PANalytical X'Pert X-ray diffractometer equipped with Cu K α radiation ($\lambda = 0.15418$ nm). Raman spectra were tested by a Raman spectrometer with a 532 nm laser excitation (DXR Smart Raman). The electrical conductivity of Ni₁₂P₅/CNTs hybrid was tested by using a four-probe resistance measuring instrument and Ni₁₂P₅/CNTs was pressed into a plate with a diameter of 12 mm and height of 0.6 mm under 15 MPa.

2.4 Electrochemical characterization

A carbon-coated Al foil was used as current collector covered by a slurry mixed with active material, CNT additives, and polyvinylidene difluoride (PVDF) (75:15:10 wt.%) in N-methyl-2-pyrrolidone (NMP). Those electrodes were cut into 12 mm-disks and dried in a vacuum oven at 60 °C for 12 h. The areal loading of sulfur was about 1.5 mg·cm⁻². The 2025-type coin cells were used and lithium foil as the anode in an Ar-filled glovebox. Celgard 2400 was chosen

as the separator. In the assembling process, 20 μ L·mg⁻¹ of 1.0 M bis(trifluoromethane)sulfonimide lithium salt (LiTFSI) in 1,3-dioxolane (DOL)/dimethoxymethane (DME) (v/v = 1:1) with 2 wt.% LiNO₃ was used as the electrolyte. Galvanostatic discharge-charge (GDC) profiles were collected by a Land CT2001A battery system between 1.7 and 2.8 V. Cyclic voltammetry (CV) was conducted on a CHI660E electrochemical workstation (CH Instruments Inc., Shanghai, China) at 0.2 mV·s⁻¹. The electrochemical impedance spectroscopy (EIS) measurements were implemented in a frequency range of 10 mHz to 100 kHz.

2.5 Computational method

Density functional theory (DFT) was carried out based on the CASTEP of Material Studio. Adsorption energy E_{ads} of Li₂S₆ group on the surface of substrate is formulated from [34]

$$E_{\text{ads}} = E_{\text{Li}_2\text{S}_6\text{-Ni}_{12}\text{P}_5/\text{CNTs}} - (E_{\text{Ni}_{12}\text{P}_5/\text{CNTs}} + E_{\text{Li}_2\text{S}_6})$$

where Li₂S₆-Ni₁₂P₅/CNTs, Ni₁₂P₅/CNTs and Li₂S₆ denote the energies of Li₂S₆ group on Ni₁₂P₅/CNTs substrate, bare Ni₁₂P₅/CNTs substrate and Li₂S₆ group.

3 Results and discussion

Ni₁₂P₅/CNTs matrix was prepared via a facile one-pot pyrolysis method. Melamine is known to be disintegrated into intermediate C₂N₂⁺, C₃N₂⁺, or C₃N₃⁺ species as carbon and nitrogen sources [35] and Ni²⁺ is reduced to metallic nickel as a catalyst to direct the growth of N-doped CNTs. At the same time, phosphorus sources released from triphenylphosphine and Ni undertook a reaction to generate Ni₁₂P₅ nanoparticles. After HCl etching, a few nickel particles remain encapsulated in the CNTs.

The SEM image given in Fig. 1(a) shows bunches of entangled carbon nanotubes, and a typical bamboo-like structure of CNT can be observed in Fig. 1(b). The diameter of CNT is under a range of 20–30 nm and the length is more than a micro long. As it shows in Figs. 1(c) and 1(d), many nanosized particles are encapsulated in the entangled carbon nanotubes with a uniform dispersion. The size range of those particles is about 5–20 nm according to TEM results. Those nanoparticles are concluded to be metal nickel and Ni₁₂P₅ as confirmed by the following XRD patterns (Fig. 2(a)). The lattice fringe of the nanoparticle in Fig. 1(d) is 0.19 nm, in accordance with (240) plane of Ni₁₂P₅. A similar morphology of Ni/CNTs can be observed from Fig. S1 in the Electronic Supplementary Material

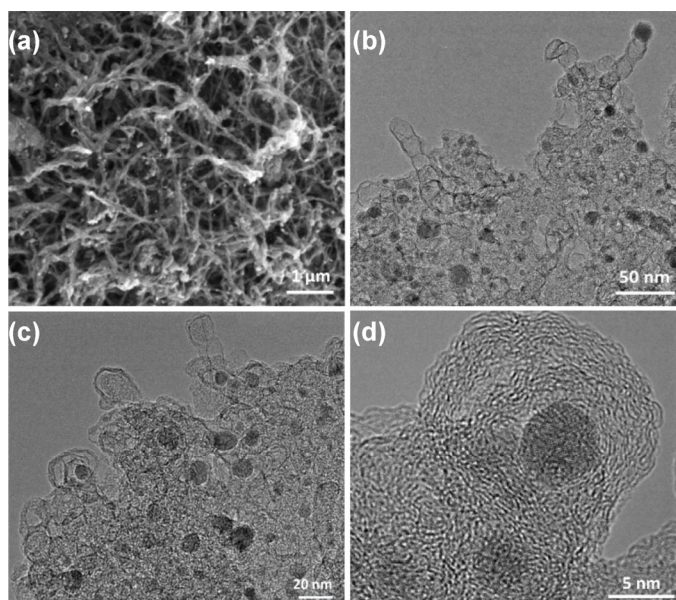


Figure 1 (a) SEM and (b)–(d) TEM images of Ni₁₂P₅/CNTs.

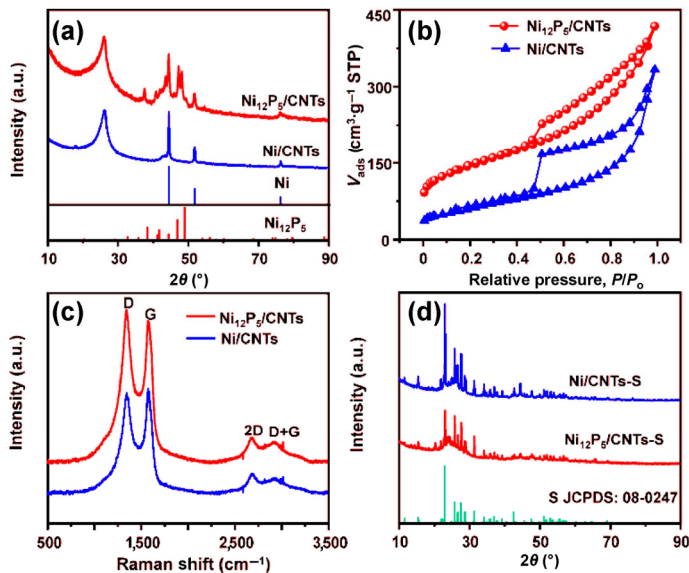


Figure 2 (a) XRD patterns, (b) N_2 adsorption–desorption isotherms (N_2 sorption isotherm is offset vertically for $30 \text{ cm}^3 \text{ g}^{-1}$ STP for $Ni_{12}P_5/CNTs$), and (c) Raman spectra of $Ni_{12}P_5/CNTs$ and $Ni/CNTs$. (d) XRD patterns of $Ni_{12}P_5/CNTs-S$ and $Ni/CNTs-S$.

(ESM) and the lattice fringe spacing of CNTs is 0.337 nm that can prove the well graphitic crystallites of CNTs.

The hybrid phase of $Ni_{12}P_5$, Ni, and CNTs can be seen in Fig. 2(a). A sharp peak centered at 26.2° indicates the (002) plane of graphitic carbon, which refers to the existence of CNTs. The peaks at 38.4° , 41.8° , 44.4° , 47.0° , and 49.0° can be identified as (112), (400), (330), (240), and (312) characteristic planes of $Ni_{12}P_5$ (JCPDS No. 74-1381), respectively, which confirms the existence of $Ni_{12}P_5$ nanoparticles. For the control sample, the peaks at 44.5° , 51.8° , and 76.4° can be classified as (111), (200), and (220) planes of Ni (JCPDS No. 04-0850), respectively, which can also be observed from the XRD pattern of $Ni_{12}P_5/CNTs$, suggesting that the co-existence of $Ni_{12}P_5$ and Ni nanoparticles. According to TG and XPS analysis results, the contents of $Ni_{12}P_5$ and Ni in $Ni_{12}P_5/CNTs$ hybrid were calculated as 8.08 wt.% and 15.57 wt.%, respectively. The presence of nickel particles can catalyze the formation of highly graphitized carbon which can increase the conductivity of CNTs.

For $Ni_{12}P_5/CNTs$ and $Ni/CNTs$, a typical type-IV isotherm and H3-type hysteresis loops can be seen in Fig. 2(b), and hierarchical pores of the host materials are presented in Fig. S2 in the ESM. After the data analysis, it is clear that the $Ni_{12}P_5/CNTs$ possesses larger SSA ($395 \text{ m}^2 \text{ g}^{-1}$) and a higher pore volume ($0.82 \text{ cm}^3 \text{ g}^{-1}$) than that of $Ni/CNTs$ ($226.0 \text{ m}^2 \text{ g}^{-1}$ and $0.55 \text{ cm}^3 \text{ g}^{-1}$, respectively). The reason for this is most probably that the decomposition of TPP during pyrolysis process can release large quantities of gases for activation leading to improve the SSA and porosity structure of $Ni_{12}P_5/CNTs$. The larger SSA, higher pore volume and hierarchical pores with 2.8 and 20.8 nm of $Ni_{12}P_5/CNTs$ are beneficial for affording sufficient space with sulfur species conversion and making the full use of the active sulfur. Raman spectra of $Ni_{12}P_5/CNTs$ and $Ni/CNTs$ (Fig. 2(c)) exhibit two intense peaks at $1,344$ and $1,582 \text{ cm}^{-1}$, respectively, which can be observed in single crystalline graphite and attributed to the in-plane bond stretching of sp^2 C pairs. The other peaks, located at $\sim 2,620$ and $2,900 \text{ cm}^{-1}$, are called 2D (D+D) and D+G bands, corresponding to the second-order of Raman spectrum in overtone and combination modes, respectively [11]. The I_D/I_G intensity ratio of $Ni_{12}P_5/CNTs$ is 1.1, higher than that of $Ni/CNTs$ (0.96), which is probably caused by that the addition of TPP can manufacture more defects on CNTs. Even so, $Ni_{12}P_5/CNTs$ maintains a high conductivity of $500 \text{ S} \cdot \text{m}^{-1}$, which is higher than that of X-72 carbon ($150 \text{ S} \cdot \text{m}^{-1}$) based on the results of the four-

probe test.

According to the thermogravimetric analysis (TGA) of two samples, the CNTs contents in $Ni_{12}P_5/CNTs$ and $Ni/CNTs$ are determined to be 69.9 wt.% and 82.9 wt.%, respectively (Fig. S3 in the ESM). XPS analysis was performed to analyze functional groups on the samples and the interaction between components. According to the XPS survey spectrum, the relative atomic contents of C, N, O, P and Ni in the $Ni_{12}P_5/CNTs$ is about 88.2%, 5.27%, 4.69%, 0.61% and 1.22%, respectively. The fitting results could be seen in Fig. S4 in the ESM. XPS analyses reveal that there are several species in $Ni_{12}P_5/CNTs$, including Ni, P species in $Ni_{12}P_5$ and C, N, O groups. After melt impregnation of the sulfur, a series of diffraction peaks of $Ni_{12}P_5/CNTs$ and $Ni/CNTs$ can be ascribed to orthorhombic α - S_8 (JCPDS No. 08-0247) indicating that sulfur is well incorporated to composite as a sulfur cathode (Fig. 2(d)). SEM images and elemental mappings of $Ni_{12}P_5/CNTs-S$ (Figs. S5–S7 in the ESM) and $Ni/CNTs-S$ (Fig. S8 in the ESM) clearly show the uniform distribution of sulfur as well as other elements, respectively. Basically, sulfur was dispersed inside of the tubes.

The electrochemical performance was investigated via assembling $Ni_{12}P_5/CNTs-S$ and $Ni/CNTs-S$ composites with 2025-coin cells. From the CV curve of $Ni_{12}P_5/CNTs-S$ (Fig. 3(a)), two cathodic peaks separately at 2.28 and 1.93 V are in accordance with the reduction of S_8 to lithium polysulfides and insoluble Li_2S_2 or Li_2S , respectively. In contrast, two anodic peaks at 2.37–2.45 V refer to the oxidation from lithium polysulfides to sulfur [36]. For $Ni/CNTs-S$, there are two cathodic peaks at 2.26 and 1.91 V, and two anodic peaks at 2.41–2.47 V, respectively. Compared to $Ni/CNTs-S$, the peaks of $Ni_{12}P_5/CNTs-S$ are sharper with a higher intensity and show a

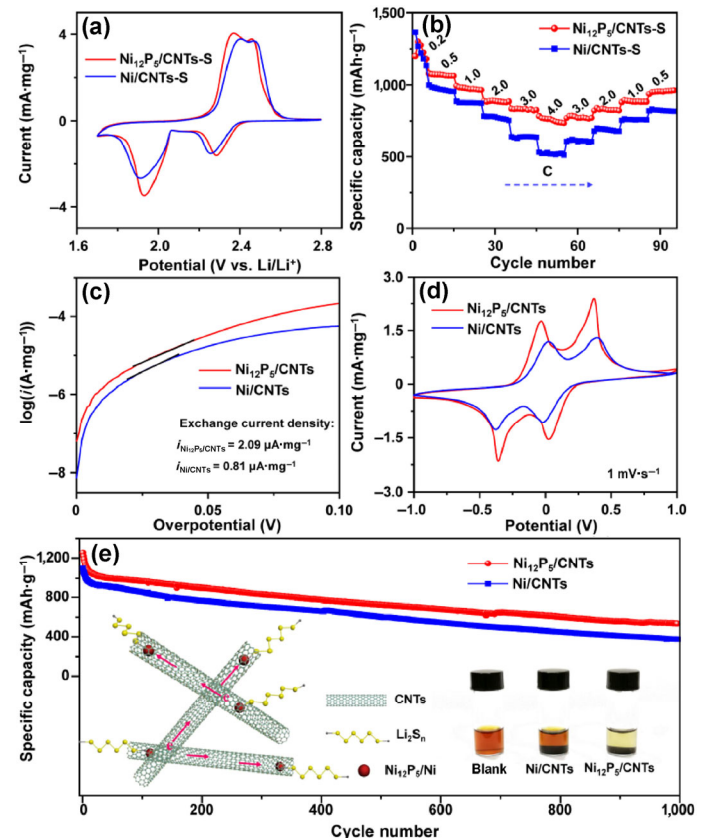


Figure 3 (a) CV curves of at $0.2 \text{ mV} \cdot \text{s}^{-1}$ and (b) rate capability at various rates of $Ni_{12}P_5/CNTs-S$ and $Ni/CNTs-S$ electrodes. (c) Tafel plots for $Ni_{12}P_5/CNTs-S$ and $Ni/CNTs-S$ electrodes in $0.2 \text{ M Li}_2\text{S}_6$ electrolyte at $0.1 \text{ mV} \cdot \text{s}^{-1}$. (d) CV curves of Li_2S_6 symmetric cells of $Ni_{12}P_5/CNTs$ and $Ni/CNTs$ electrodes at $1 \text{ mV} \cdot \text{s}^{-1}$. (e) Long cycling performances of $Ni_{12}P_5/CNTs-S$ and $Ni/CNTs-S$ electrodes over 1,000 cycles at 0.5 C. The inset is optical photo of $Ni_{12}P_5/CNTs$ and $Ni/CNTs$ after Li_2S_6 adsorption.

higher onset reduction potential and a lower onset oxidation potential, suggesting that faster electrochemical reactions occurred in the Ni₁₂P₅/CNTs-S electrode. As displayed in Fig. 3(b), the specific discharge capacity of Ni₁₂P₅/CNTs-S varies from 1,079 to 784 mAh·g⁻¹ when the C rate increases from 0.5 to 4.0 C (1 C = 1,675 mA·g⁻¹), respectively. Even at 4 C, Ni₁₂P₅/CNTs-S cathode can achieve a capacity of 784 mAh·g⁻¹, higher than that of Ni/CNTs-S cathode (636 mAh·g⁻¹). Furthermore, when the C rate returns to 0.5 C, the Ni₁₂P₅/CNTs-S cathode is able to recover more capacity than the Ni/CNTs-S cathode. The good rate capability of Ni₁₂P₅/CNTs-S cathode may lie in rapid electron transfer and catalytic synergistic effect of co-existence of Ni₁₂P₅ and Ni on the sulfur redox process.

We further test the catalytic effects of Ni₁₂P₅/CNTs and Ni/CNTs electrodes referring to a method reported by the literature [37]. The higher scanning current densities in linear sweep voltammograms (Figs. S9(a) and S9(b) in the ESM) and the higher exchange current density in Tafel plots (Fig. 3(c)) of Ni₁₂P₅/CNTs than those of Ni/CNTs electrode confirm the enhanced reaction kinetics for LiPS redox reactions by Ni₁₂P₅. From CV curves of Li₂S₆ symmetric cells (Fig. 3(d)), the higher redox current of Ni₁₂P₅/CNTs suggests enhanced redox of polysulfides by Ni₁₂P₅. These analyses are in accordance with CV results demonstrating that Ni₁₂P₅/CNTs-S electrode exhibiting fast redox reactions are attributed to the improved kinetics of polysulfide redox reactions by Ni₁₂P₅. As shown in Fig. S9(c) in the ESM, GDC curves of Ni₁₂P₅/CNTs-S have two apparent plateaus, which are in line with the CV results. The charge transfer resistance (R_{ct}) of Ni₁₂P₅/CNTs-S is much lower than that of Ni/CNTs-S, indicating the enhanced conduction of electrons and Li ions of Ni₁₂P₅/CNTs-S as testified by the EIS measurements (Fig. S9(d) in the ESM).

The long-cycle performances of Ni₁₂P₅/CNTs-S and Ni/CNTs-S with a sulfur content of 65 wt.% are shown in Fig. 3(e), demonstrating that Ni₁₂P₅/CNTs-S composite has a superior capability with an initial capacity of 1,256 mAh·g⁻¹ at 0.5 C and 533 mAh·g⁻¹ remained over 1,000 cycles, higher than that of Ni/CNTs-S (375 mAh·g⁻¹). The rate capability and cycling performance are favorable in comparison with other host materials reported previously for Li-S batteries (Table S1 in the ESM). The cycling performance of Ni₁₂P₅/CNTs-S cathode with a high sulfur loading of 3.0 mg·cm⁻² is displayed in Fig. S10 in the ESM. It maintains a capacity of 770 mAh·g⁻¹ after 50 cycles at 0.2 C including 78 wt.% sulfur. Raman spectra of Ni₁₂P₅/CNTs-S and XRD pattern of Ni₁₂P₅/CNTs-S after the sulfur was washed out by CS₂ both demonstrate that Ni was not transferred into NiS_x during sulfur loading process (Fig. S11 in the ESM). From the inset picture of Fig. 3(e), the brown yellow Li₂S₆ solution containing Ni₁₂P₅/CNTs became pale yellow after 24 h, while the solution containing the same amount of Ni/CNTs still kept brown yellow, indicating that Ni₁₂P₅/CNTs has stronger adsorption capacity to Li₂S₆ than Ni/CNTs. Therefore, Ni₁₂P₅/CNTs-sulfur cathode can obtain a more stable and long cycling life.

In order to study the adsorption capability of Ni₁₂P₅/CNTs to Li₂S₆, we prepared a series of Li₂S₆ solution with different concentration for UV-vis test (Fig. 4(a)) via a typical method [38]. A calibration curve was proposed to determine the concentration of Li₂S₆ from 0.5 to 1.75 mM (Fig. 4(b)), which shows a linear relationship between absorbance and concentration at 450 nm. The absorptivity of Ni₁₂P₅/CNTs and Ni/CNTs was counted by the formula $Y = 2.002x$, respectively, and the correlation coefficient was 0.999. The absorbed Li₂S₆ concentration of Ni₁₂P₅/CNTs is about threefold than that of Ni/CNTs, convincingly suggesting that Ni₁₂P₅/CNTs can bind Li₂S₆ effectually in the electrolyte. The strong interaction between Ni₁₂P₅ and Li₂S₆ was also confirmed by theoretical calculation based on the DFT calculations (Figs. 4(c) and 4(d)). The adsorption energy (E_{ads}) of Li₂S₆ on the surface (312) of Ni₁₂P₅ is calculated to be -4.977 eV (Table S2 in the ESM), which is greater than that of common carbon (0.5 eV). Accordingly, both theoretical and experimental studies suggest that Ni₁₂P₅/CNTs has firm affinity for Li₂S₆ solution.

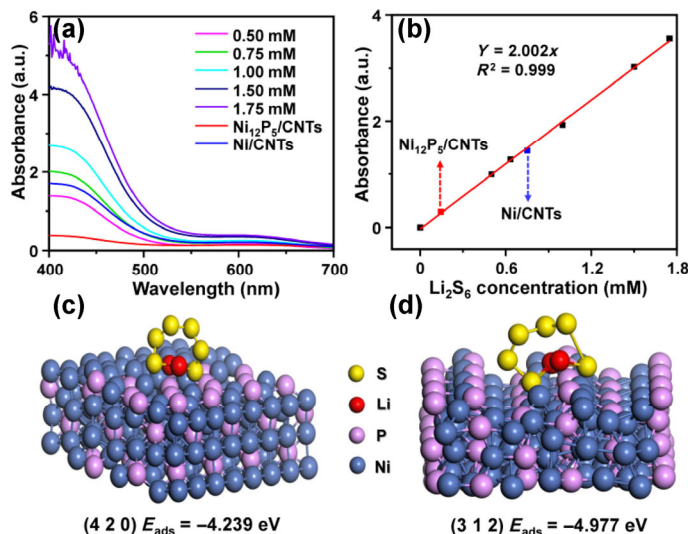


Figure 4 (a) UV-vis spectra of Li₂S₆ solution from 0.5 to 1.75 mM. (b) Linear calibration of the absorbance at 450 nm of Li₂S₆ solution from 0.5 to 1.75 mM. Geometry of Li₂S₆ binding on the (c) (420) and (d) (312) plane of Ni₁₂P₅.

That is to say, the presence of Ni₁₂P₅ is beneficial for the fast electron transport and the inhibition of migratory polysulfides, resulting in high rate and long-life Li-S batteries.

4 Conclusions

In summary, we have developed a simple way to prepare Ni₁₂P₅/CNTs composite as a sulfur host with a highly conductive property and high affinity with LiPS to enhance the rate capability and cycling durability of Li-S batteries. On the one hand, the presence of polar Ni₁₂P₅ with strong affinity for LiPS and enhanced kinetics of LiPS redox reaction is beneficial for suppressing the shuttle effect and enhancing cycling capability of Li-S cells. On the other hand, 1D carbon nanotubes containing conductive Ni and Ni₁₂P₅ nanoparticles with a high specific area make a positive contribution to the formation of a conductive network, speeding up the transfer of electrons. Benefiting from the well-designed structure including such a conductive framework with strong chemisorption on LiPS, the Ni₁₂P₅/CNTs-S cathode achieves a high rate capacity and long-cycle lifespan. This work will provide significant insight for the metal-rich phosphides incorporated in sulfur hosts as promising cathodes for lithium sulfur batteries.

Acknowledgements

The authors are grateful to the financial support by the National Natural Science Foundation of China (Nos. 21776041 and 21875028), and Cheung Kong Scholars Programme of China (No. T2015036).

Electronic Supplementary Material: Supplementary material (SEM images and EDS elemental mappings of Ni₁₂P₅/CNTs-S and Ni/CNTs; TEM images and TGA curves of Ni₁₂P₅/CNTs and Ni/CNTs, etc.) is available in the online version of this article at <https://doi.org/10.1007/s12274-019-2381-0>.

References

- Armand, M.; Tarascon, J. M. Building better batteries. *Nature* **2008**, *451*, 652–657.
- Manthiram, A.; Fu, Y. Z.; Chung, S. H.; Zu, C. X.; Su, Y. S. Rechargeable lithium-sulfur batteries. *Chem. Rev.* **2014**, *114*, 11751–11787.
- Yin, Y. X.; Xin, S.; Guo, Y. G.; Wan, L. J. Lithium-sulfur batteries: Electrochemistry, materials, and prospects. *Angew. Chem., Int. Ed.* **2013**, *52*, 13186–13200.
- Goodenough, J. B.; Kim, Y. Challenges for rechargeable Li batteries.

- Chem. Mater.* **2010**, *22*, 587–603.
- [5] Larcher, D.; Tarascon, J. M. Towards greener and more sustainable batteries for electrical energy storage. *Nat. Chem.* **2015**, *7*, 19–29.
- [6] Urbonaite, S.; Poux, T.; Novák, P. Progress towards commercially viable Li–S battery cells. *Adv. Energy Mater.* **2015**, *5*, 1500118.
- [7] Yang, Y.; Zheng, G. Y.; Cui, Y. Nanostructured sulfur cathodes. *Chem. Soc. Rev.* **2013**, *42*, 3018–3032.
- [8] Moon, S.; Jung, Y. H.; Jung, W. K.; Jung, D. S.; Choi, J. W.; Kim, D. K. Encapsulated monoclinic sulfur for stable cycling of Li–S rechargeable batteries. *Adv. Mater.* **2013**, *25*, 6547–6553.
- [9] Zhang, S. S. Liquid electrolyte lithium/sulfur battery: Fundamental chemistry, problems, and solutions. *J. Power Sources* **2013**, *231*, 153–162.
- [10] Zhang, Z.; Wu, D. H.; Zhou, Z.; Li, G. R.; Liu, S.; Gao, X. P. Sulfur/nickel ferrite composite as cathode with high-volumetric-capacity for lithium-sulfur battery. *Sci. China Mater.* **2019**, *62*, 74–86, DOI: 10.1007/s40843-018-9292-7.
- [11] He, B.; Li, W. C.; Yang, C.; Wang, S. Q.; Lu, A. H. Incorporating sulfur inside the pores of carbons for advanced lithium–sulfur batteries: An electrolysis approach. *ACS Nano* **2016**, *10*, 1633–1639.
- [12] Zhao, M. Q.; Zhang, Q.; Huang, J. Q.; Tian, G. L.; Nie, J. Q.; Peng, H. J.; Wei, F. Unstacked double-layer templated graphene for high-rate lithium–sulphur batteries. *Nat. Commun.* **2014**, *5*, 3410.
- [13] Hu, G. J.; Xu, C.; Sun, Z. H.; Wang, S. G.; Cheng, H. M.; Li, F.; Ren, W. C. 3D graphene-foam-reduced-graphene-oxide hybrid nested hierarchical networks for high-performance Li–S batteries. *Adv. Mater.* **2016**, *28*, 1603–1609.
- [14] Zhao, M. Q.; Peng, H. J.; Tian, G. L.; Zhang, Q.; Huang, J. Q.; Cheng, X. B.; Tang, C.; Wei, F. Hierarchical vine-tree-like carbon nanotube architectures: *In-situ* CVD self-assembly and their use as robust scaffolds for lithium-sulfur batteries. *Adv. Mater.* **2014**, *26*, 7051–7058.
- [15] Zhao, Y.; Wu, W.; Li, J.; Xu, Z.; Guan, L. Encapsulating MWNTs into hollow porous carbon nanotubes: A tube-in-tube carbon nanostructure for high-performance lithium-sulfur batteries. *Adv. Mater.* **2014**, *26*, 5113–5118.
- [16] Zhang, X. Q.; He, B.; Li, W. C.; Lu, A. H. Hollow carbon nanofibers with dynamic adjustable pore sizes and closed ends as hosts for high-rate lithium-sulfur battery cathodes. *Nano Res.* **2018**, *11*, 1238–1246.
- [17] Zhou, G. M.; Li, L.; Wang, D. W.; Shan, X. Y.; Pei, S. F.; Li, F.; Cheng, H. M. Flexible sulfur-graphene-polypropylene separator integrated electrode for advanced Li–S batteries. *Adv. Mater.* **2015**, *27*, 641–647.
- [18] Sun, Q.; He, B.; Zhang, X. Q.; Lu, A. H. Engineering of hollow core–shell interlinked carbon spheres for highly stable lithium–sulfur batteries. *ACS Nano* **2015**, *9*, 8504–8513.
- [19] Zhang, L. H.; He, B.; Li, W. C.; Lu, A. H. Surface free energy-induced assembly to the synthesis of grid-like multicavity carbon spheres with high level in-cavity encapsulation for Lithium–Sulfur cathode. *Adv. Energy Mater.* **2017**, *7*, 1701518.
- [20] Li, D.; Han, F.; Wang, S.; Cheng, F.; Sun, Q.; Li, W. C. High sulfur loading cathodes fabricated using peapodlike, large pore volume mesoporous carbon for Lithium–Sulfur battery. *ACS Appl. Mater. Interfaces* **2013**, *5*, 2208–2213.
- [21] Song, J. X.; Gordin, M. L.; Xu, T.; Chen, S. R.; Yu, Z. X.; Sohn, H.; Lu, J.; Ren, Y.; Duan, Y. H.; Wang, D. H. Strong lithium polysulfide chemisorption on electroactive sites of nitrogen-doped carbon composites for high-performance lithium–sulfur battery cathodes. *Angew. Chem., Int. Ed.* **2015**, *127*, 4399–4403.
- [22] Yang, C. P.; Yin, Y. X.; Ye, H.; Jiang, K. C.; Zhang, J.; Guo, Y. G. Insight into the effect of boron doping on sulfur/carbon cathode in lithium–sulfur batteries. *ACS Appl. Mater. Interfaces* **2014**, *6*, 8789–8795.
- [23] Zhou, G. M.; Yin, L. C.; Wang, D. W.; Li, L.; Pei, S. F.; Gentle, I. R.; Li, F.; Cheng, H. M. Fibrous hybrid of graphene and sulfur nanocrystals for high-performance Lithium–Sulfur batteries. *ACS Nano* **2013**, *7*, 5367–5375.
- [24] Pang, Q.; Tang, J. T.; Huang, H.; Liang, X.; Hart, C.; Tam, K. C.; Nazar, L. F. A nitrogen and sulfur dual-doped carbon derived from polyrhodanine@cellulose for advanced lithium-sulfur batteries. *Adv. Mater.* **2015**, *27*, 6021–6028.
- [25] Gu, X. X.; Tong, C. J.; Lai, C.; Qiu, J. X.; Huang, X. X.; Yang, W. L.; Wen, B.; Liu, L. M.; Hou, Y. L.; Zhang, S. Q. A porous nitrogen and phosphorous dual doped graphene blocking layer for high performance Li–S batteries. *J. Mater. Chem. A* **2015**, *3*, 16670–16678.
- [26] Liang, X.; Hart, C.; Pang, Q.; Garsuch, A.; Weiss, T.; Nazar, L. F. A highly efficient polysulfide mediator for lithium–sulfur batteries. *Nat. Commun.* **2015**, *6*, 5682.
- [27] Seh, Z. W.; Li, W. Y.; Cha, J. J.; Zheng, G. Y.; Yang, Y.; McDowell, M. T.; Hsu, P. C.; Cui, Y. Sulphur–TiO₂ yolk–shell nanoarchitecture with internal void space for long-cycle lithium–sulphur batteries. *Nat. Commun.* **2013**, *4*, 1331.
- [28] Li, C. X.; Xi, Z. C.; Guo, D. X.; Chen, X. J.; Yin, L. W. Chemical immobilization effect on Lithium polysulfides for lithium–sulfur batteries. *Small* **2018**, *14*, 1701986.
- [29] Ma, L. B.; Chen, R. P.; Zhu, G. Y.; Hu, Y.; Wang, Y. R.; Chen, T.; Liu, J.; Jin, Z. Cerium oxide nanocrystal embedded bimodal micromesoporous nitrogen-rich carbon nanospheres as effective sulfur host for lithium-sulfur batteries. *ACS Nano* **2017**, *11*, 7274–7283.
- [30] Wang, H. Q.; Zhang, W. C.; Xu, J. Z.; Guo, Z. P. Advances in polar materials for lithium–sulfur batteries. *Adv. Funct. Mater.* **2018**, *28*, 1707520.
- [31] Tao, X. Y.; Wang, J. G.; Liu, C.; Wang, H. T.; Yao, H. B.; Zheng, G. Y.; Seh, Z. W.; Cai, Q. X.; Li, W. Y.; Zhou, G. M. et al. Balancing surface adsorption and diffusion of lithium-polysulfides on nonconductive oxides for lithium-sulfur battery design. *Nat. Commun.* **2016**, *7*, 11203.
- [32] Xu, Y. Y.; Duan, S. B.; Li, H. Y.; Yang, M.; Wang, S. J.; Wang, X.; Wang, R. M. Au/Ni₁₂P₃ core/shell single-crystal nanoparticles as oxygen evolution reaction catalyst. *Nano Res.* **2017**, *10*, 3103–3112.
- [33] Shi, Y. M.; Zhang, B. Recent advances in transition metal phosphide nanomaterials: Synthesis and applications in hydrogen evolution reaction. *Chem. Soc. Rev.* **2016**, *45*, 1529–1541.
- [34] Ji, P. H.; Shang, B.; Peng, Q. M.; Hu, X. B.; Wei, J. W. α -MoO₃ spheres as effective polysulfides adsorbent for high sulfur content cathode in lithium-sulfur batteries. *J. Power Sources* **2018**, *400*, 572–579.
- [35] Balamurugan, J.; Thanh, T. D.; Kim, N. H.; Lee, J. H. Facile synthesis of 3D hierarchical N-doped graphene nanosheet/cobalt encapsulated carbon nanotubes for high energy density asymmetric supercapacitors. *J. Mater. Chem. A* **2016**, *4*, 9555–9565.
- [36] Zhou, T. H.; Lv, W.; Li, J.; Zhou, G. M.; Zhao, Y.; Fan, S. X.; Liu, B. L.; Li, B. H.; Kang, F. Y.; Yang, Q. H. Twinborn TiO₂–TiN heterostructures enabling smooth trapping-diffusion-conversion of polysulfides towards ultralong life lithium-sulfur batteries. *Energy Environ. Sci.* **2017**, *10*, 1694–1703.
- [37] Xu, Z. L.; Lin, S. H.; Onofrio, N.; Zhou, L. M.; Shi, F. Y.; Lu, W.; Kang, K.; Zhang, Q.; Lau, S. P. Exceptional catalytic effects of black phosphorus quantum dots in shuttling-free lithium sulfur batteries. *Nat. Commun.* **2018**, *9*, 4164.
- [38] He, B.; Li, W. C.; Zhang, Y.; Yu, X. F.; Zhang, B. S.; Li, F.; Lu, A. H. Paragenesis BN/CNTs hybrid as a monoclinic sulfur host for high rate and ultra-long life lithium–sulfur battery. *J. Mater. Chem. A* **2018**, *6*, 24194–24200, DOI: 10.1039/C8TA09564G.